ACS Catalysis

pubs.acs.org/acscatalysis Research Article

Active and Stable Pt−Ni Alloy Octahedra Catalyst for Oxygen Reduction via Near-Surface Atomical Engineering

Fanpeng Kong,# Zhouhong Ren,# Mohammad Norouzi Banis,# Lei Du, Xin Zhou, Guangyu Chen, Lei Zhang, Junjie Li, Sizhe Wang, Minsi Li, Kieran Doyle-Davis, Yulin Ma, Ruying Li, Alan Young, Lijun Yang, Matthew Markiewicz, Yujin Tong, Geping Yin, Chunyu Du,* Jun Luo,* and Xueliang Sun*

Cite This: *ACS Catal.* 2020, 10, 4205−4214 Read Online

ACCESS | Metrics & More | Article Recommendations | Supporting Information

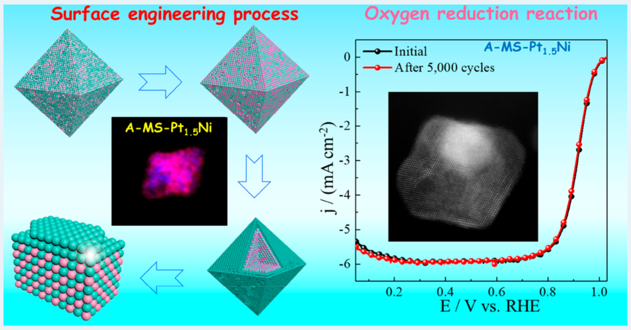

ABSTRACT: Shape-controlled Pt-based bimetallic nanocrystals with ultrathin Pt-rich surfaces are appealing electrocatalysts for some key electrochemical reactions such as the oxygen reduction reaction (ORR) because of the synergistic tuning of topological atom configuration and strengthened electronic effects. However, it is rather challenging to fabricate such particular structures that can remain intact in harsh electrochemical environments, as such Pt-based nanocatalysts are unable to simultaneously achieve both unparalleled activity and robust stability. Here, a facile surface engineering strategy is proposed and employed to atomically tailor the near-surface structure of the $Pt_{1.5}Ni$ octahedra. The engineered Pt−Ni octahedra consist of an ultrathin Pt-rich shell (∼two atomic layers) and Pt-rich bulk composition. The optimized octahedral catalyst exhibits superior specific and mass activity (7.7 $mA/cm^2{}_{Pt}$ and 1.9 A/mg_{Pt} at 0.9 V) for ORR, ∼20 and ∼10 times higher than commercial Pt/C, respectively. The ligand and strain effects arising from the near-surface engineering are unraveled to be responsible for the remarkable ORR activity. Moreover, it shows robust stability with just 9.2% decay in mass activity after accelerated degradation tests (ADTs), as its compositional nature prevents surface Pt atoms and interior Ni atoms from diffusion and dissolution, compared with a decrease of 33% for commercial Pt/C. Our atomical engineered surface strategy illustrates a facile and effective design for a class of Pt-based nanocatalysts with excellent activity and stability.

KEYWORDS: *oxygen reduction reaction, atomic surface engineering, surface structure, stability, electronic structure*

INTRODUCTION

Oxygen surface chemistry is playing a pivotal role in energy storage and conversion devices (e.g., (cogeneration) fuel cells, metal−air batteries, and electrolyzers). In particular, one focus is the oxygen reduction reaction (ORR), which has sluggish kinetics in proton exchange membrane fuel cells[1−4] and has triggered intense research in the past decade. Although highly dispersed Pt nanoparticles (NPs) are the most widely explored ORR catalysts, substantial improvement in activity and a subsequent reduction of Pt usage are required because of the scarcity of Pt resources and its high cost.[5−15] Because of the high surface sensitivity of ORR, its activity on Pt depends largely on the topological atom configuration and the electronic structure of the top Pt layers.[16,17] The surface atom configuration of Pt is directly related to the exposed crystallography faces, which is mainly achieved by the shape control of Pt nanocrystals.[18,19] Previous studies have shown that the kinetics of the ORR on specific shape-controlled Pt nanoparticles can be greatly boosted.[20] Meanwhile, the electronic structure of surface Pt atoms can be tailored by the varied underlying subsurfaces,[21,22] which are intentionally or unintentionally formed by coating the Pt shell or chemical/electrochemical dealloying.[23−27] This tailoring, mainly through the so-called geometric effect and ligand effect originating from the lattice mismatch and heterometallic interaction, is rather effective but decays quickly with the thickness of Pt overlayers.[28−31] Thus, forming an ultrathin Pt-rich surface is a prerequisite for efficiently tuning its ORR activity.

Reasonably, combining shape control and an ultrathin Pt-rich surface would promise unprecedented ORR properties through a synergistic effect. Pt_3Ni (111) with a Pt surface and a Ni-rich subsurface layer was found to exhibit a 90-fold enhancement in ORR activity compared with Pt/C.[32] This pioneering work leads to extensive follow-up studies on shape-

Received: November 26, 2019
Revised: March 12, 2020
Published: March 13, 2020

https://dx.doi.org/10.1021/acscatal.9b05133
ACS Catal. 2020, 10, 4205−4214

controlled Pt-based nanocrystals.[33−38] Strasser et al. demonstrated that shape-selective PtNi octahedra with a Pt-rich surface of two to three atom layers fabricated by electrochemical leaching exhibit exceptional ORR activity.[37] These PtNi octahedra, however, suffer from poor long-term stability because of the massive dissolution of interior Ni atoms, which has been commonly observed for other Pt-based binary systems.[39−41] High-temperature annealing to form denser Pt surfaces/intermetallic compounds and increasing Pt content are helpful for improving the stability of Pt-based binary nanocrystals.[11,39,42,43] Nevertheless, high-temperature treatment often leads to the collapse of controlled shapes,[44] while increasing the Pt ratio causes severely decreased mass activity because of the formation of thick Pt-rich layers.[37] Thus, the synthesis of Pt-based nanocrystals with both controlled shape and an ultrathin Pt-rich surface to simultaneously enhance the activity and stability still remains a great challenge.

In this paper, a facile (near-) surface engineering strategy is proposed to atomically tune the surface/near-surface structure of octahedral $Pt_{1.5}Ni$ nanocatalysts. This tuning process is achieved on the basis of the controlled reduction and inward infiltration of Ni atoms, leading to an ultrathin (~two atomic layers) Pt-rich shell coated on the unaffected interior. Modulated by the underlying Pt−Ni alloy, the Pt shell presents outstanding ORR activity and robust stability. The mass and specific ORR activity of the modified Pt−Ni electrocatalyst shows ~10 and ~20× enhancement compared with commercial Pt/C. In addition, the loss of performance after ADTs is only 9.2% compared with a loss of 33% for commercial Pt/C. The origin of this performance enhancement is carefully elucidated by synchrotron-based X-ray photoelectron spectroscopy (XPS), X-ray absorption fine structure (XAFS) analysis, and density functional theory (DFT) calculations.

■ EXPERIMENTAL SECTION

Materials. Platinum acetylacetone ($Pt(acac)_2$, Aladdin), nickel acetylacetone ($Ni(acac)_2$, Aladdin), dimethylformamide (DMF, Aladdin), benzoic acid (C_6H_5COOH, Alfa Aesar), nickel nitrate hexahydrate ($Ni(NO_3)_2 \cdot 6H_2O$, Aladdin), carbon powder (Vulcan XC-72R, Cabot Corporation), perchloric acid ($HClO_4$, Aladdin), hydrochloric acid (HCl, Aladdin), nitric acid (HNO_3, Aladdin), commercial Pt/C (20 wt % loading, Johnson Matthey), and isopropanol (C_3H_8O, Sinopharm Chemical Reagent) were used without any further purification. Nafion solution (5.0 wt %) was purchased from Dupont to prepare the thin film electrode. Deionized water (18.2 MΩ, Mill-Q Corporation) was used for preparing the solutions.

Preparation of $Pt_{1.5}Ni$ and $Pt_{1.0}Ni$ Octahedra on Carbon Supports. Initially, 40 mg of Vulcan XC-72R carbon was dispersed in 30 mL of DMF under ultrasonic agitation for 30 min. $Pt(acac)_2$ (20 mg), $Ni(acac)_2$ (10 mg), and C_6H_5COOH (120 mg) were then added step by step into the above carbon suspension, followed by another 15 min of ultrasonic dispersion. The final mixture was transferred into a 50 mL Teflon-lined high pressure vessel, which was then heated up to 160 °C and maintained for 24 h. After that, the obtained $Pt_{1.5}Ni$ sample was collected, washed with ethanol and deionized water, and dried under vacuum at 70 °C for 12 h. The Pt_1Ni_1 nanoparticles were synthesized by increasing the mass of $Ni(acac)_2$ to 13 mg.

Near-Surface Modification of $Pt_{1.5}Ni$ (Denoted as MS-$Pt_{1.5}Ni$). First, 40 mg of $Pt_{1.5}Ni/C$ catalyst and an additional 2.5 mg of $Ni(NO)_3 \cdot 6H_2O$ were ultrasonically dispersed in 10 mL of deionized water. The homogeneous mixture was immediately frozen by using liquid nitrogen and dried in a refrigerated drying chamber. The sample was then calcined under 20% H_2/Ar atmosphere at 150 °C for 2 h to obtain the final MS-$Pt_{1.5}Ni$ nanocatalyst.

Preparation of A-$Pt_{1.5}Ni$, A-MS-$Pt_{1.5}Ni$, and A-$Pt_{1.0}Ni$. The as-prepared $Pt_{1.5}Ni$, Pt_1Ni_1, and MS-$Pt_{1.5}Ni$ were respectively dispersed in 50 mL of 0.1 M $HClO_4$ and stirred overnight at 60 °C. The products were collected by centrifugation and washed four times with deionized water.

Physical Characterization. Transmission electron microscopy (TEM), high-resolution TEM (HR-TEM), high angle annular dark field-scanning transmission electron microscopy (HAADF-STEM), and energy dispersive X-ray spectroscopy (EDS) were carried out on an FEI Tecnai G2F30 with an acceleration voltage of 300 kV. Atomic resolved HAADF-STEM images were collected on an FEI Titan Cubed Themis G2 300. Cu grids were used during all the EDS analyses. X-ray photoelectron spectroscopy (XPS) was performed on a PHI 5700 ECSA system using Al Kα radiation (1486.6 eV). Powder X-ray diffraction (XRD) was carried out on a Rigaku D/max−γA X-ray diffractometer with Cu Kα radiation (λ = 1.54178 Å). The composition of catalysts was determined by a PerkinElmer Optima 5300DV inductively coupled plasma (ICP) instrument. Ten milligrams of catalyst was digested in 20 mL of aqua regia followed by stirring for more than 12 h, which was then diluted to 100 mL by deionized water as the testing sample. Synchrotron-based XPS was conducted on the variable line spacing plane grating monochromator (VLS-PGM) 11ID-2 beamline at the Canadian Light Source (CLS), where the photon energy was set at 160 eV. Pt L_2-edge- and Pt L_3-edge- X-ray absorption fine structure (XAFS) spectra were collected on the hard X-ray microanalysis (HXMA) beamline at the CLS 06ID-01. The primary beamline optics include a 1.2 m water-cooled silicon, a liquid-nitrogen-cooled double crystal monochromator (Kohzu CMJ-1), and a 1.15 m long water-cooled silicon toroidal focusing mirror (separate Rh and Pt coating stripes). Ni K edge XAFS spectra were tested on soft X-ray micro characterization beamline (SXRMB) 06B1-1 at CLS. The SXRMB endstation is equipped with a double-crystal monochromator with two sets of interchangeable crystals and the operating energy range is from 1.7 to 10 keV.

X-ray absorption near edge structure (XANES), extended X-ray absorption fine structure (EXAFS) data reduction, and EXAFS fitting were carried out using the IFEFFIT-based programs Athena and Artemis.[45] Edge step normalization for each spectrum was performed by subtracting the pre-edge and postedge backgrounds in Athena. White line (WL) intensity analysis was conducted on the basis of the previous research.[46,47] In this method, the WL intensity of Pt L_2- and L_3-edges was obtained by subtracting the Pt $L_{2,3}$ edge (XANES) from the corresponding XANES of Au. The area under the difference curve was integrated between the two vertical bars, and $\triangle A_3$ and $\triangle A_2$ were calculated using the following expressions:

$$\triangle A_3 = \int \mu(\mathrm{Pt})_{L_3\mathrm{WL}} - \int \mu(\mathrm{Au})_{L_3\mathrm{WL}}$$

$$\triangle A_2 = \int \mu(\mathrm{Pt})_{L_2\mathrm{WL}} - \int \mu(\mathrm{Au})_{L_2\mathrm{WL}}$$

According to Sham et al.,[48] $\triangle A_3$ and $\triangle A_2$ are related to the following theoretical expressions:

$$\triangle A_3 = C_0 N_0 E_3 (R_d^{2p_{3/2}})^2 \left[\frac{6h_{5/2} + h_{3/2}}{15}\right]$$

$$\triangle A_2 = C_0 N_0 E_2 (R_d^{2p_{1/2}})^2 \left(\frac{1}{3} h_{3/2}\right)$$

where $C_0 = 4\pi r^2 \alpha/3$ (α is the fine structure constant), N_0 is the density of Pt atoms, h_j is the j (j = 3d or 5d) hole counts, R is the radial transition matrix element, and E_2 and E_3 are the corresponding edge thresholds (E_0) for the L_2 and L_3 edges, respectively. By assuming that the R terms are similar for both edges

$$C = C_0 N_0 R^2$$

and this approximation

$$h_{5/2} = \frac{1}{2C}\left[5\frac{E_2}{E_3}\triangle A_3 - \triangle A_2\right]$$

$$h_{3/2} = \left[\frac{3\triangle A_2}{C}\right]$$

The C value for these equations was 7.484×10^4 cm^{-1}.[46,47]

Electrochemical Testing. Four milligrams of the catalyst was dispersed in a solvent including 3 mL of deionized water, 1 mL of isopropanol, and 4 μL of Nafion by sonication for 10 min (catalyst concentration: 1 mg mL^{-1}). Ten microliters of the catalyst ink was dropped on a rotating disk glassy carbon electrode (5 mm in diameter), which was already polished by 0.3 μm alumina powder in advance. The Pt loadings for commercial Pt/C, A-$Pt_{1.5}Ni$, A-$Pt_{1.0}Ni$, and A-MS-$Pt_{1.5}Ni$ are 10.2, 7.65, 7.65, and 7.65 μg_{Pt} cm^{-2}, respectively. Pt foil and Ag/AgCl were used as the counter electrode and reference electrode, respectively. Cyclic voltammetry (CV) curves were recorded in an argon-saturated 0.1 M $HClO_4$ solution at a scan rate of 50 mV s^{-1}. The oxygen reduction performance was tested by linear sweep voltammogram at a scan rate of 10 mV s^{-1} using a rotating disk electrode in oxygen saturated 0.1 M $HClO_4$ solution. The adsorption of monolayer CO was achieved by immersing the working electrode in CO-saturated 0.1 M perchloric acid electrolyte for 20 min, followed by purging the electrolyte with argon and holding the working electrode at 0.4 V for 30 min. The adsorbed CO was subsequently stripped from surface by a potential sweep at a rate of 50 mV s^{-1}. The ADTs were performed by applying 5000 and 10 000 potential cycles between 0.6 and 1.0 V at a scan rate of 50 mV s^{-1}. All the electrochemical measurements were conducted on a CHI 604D electrochemical workstation at room temperature, and the potentials were reported with respect to the reversible hydrogen electrode (RHE).

DFT Calculation. All the DFT calculations were performed using the Vienna Ab-initio Simulation Package (VASP),[49,50] employing the DFT and the Projected Augmented Wave (PAW) method.[51] The Perdew−Burke−Ernzerhof (PBE) functional was used to describe the exchange and correlation effect.[52] For all the geometry optimizations, the cutoff energy was set to be 400 eV. The Monkhorst−Pack grids[53] were set to be 9 × 9 × 9 and 5 × 5 × 1 for performing the bulk and surface optimization calculations, respectively. The surface models for adsorption energy calculation were constructed as seven-layer 2 × 2 slab, where two-layer Pt (2 ML) and five-layer Pt (5 ML) were arranged on the top and the $Pt_{1.5}Ni$ were arranged in the bottom, respectively. The surface models for vacancy formation energy calculation were constructed as seven-layer 2 × 2 slab, where two-layer Pt were arranged on the top and five-layer $Pt_{1.5}Ni$ and PtNi were arranged in the bottom. To simulate the OH adsorption, only the adsorption on the top site of Pt was considered, since previous work has found that OH could be stabilized by water on the top site.[27]

The vacancy formation energy of surface Pt and third layer Ni was defined as

$$E_{VPt} = E_{slab-VPt} + \mu_{Pt} - E_{slab}$$

$$E_{VNi} = E_{slab-VNi} + \mu_{Ni} - E_{slab}$$

where E_V is the vacancy formation energy, $E_{slab\text{-}V}$ is the electronic energy of the surface with one vacancy, μ is the chemical potential of one Pt (Ni) atom, and E_{slab} is the electronic energy of intact slab. Under this definition, a lower value indicates a higher possibility to generate a vacancy.

RESULTS

Octahedral $Pt_{1.5}Ni$ nanoparticles were prepared using a facile surfactant-free solvothermal method.[27,37] TEM imaging (Figure S1a) reveals that the $Pt_{1.5}Ni$ nanoparticles are highly dispersed on the carbon support. The representative HR-TEM image shown in Figure S1b clearly demonstrates the well-defined octahedral morphology. Their element composition is determined as $Pt_{60}Ni_{40}$ by ICP-OES shown in Table S1, and the near-surface composition is revealed as $Pt_{70}Ni_{30}$ on the basis of XPS (Figure S2 and Figure S3), indicating that the near-surface is Pt-segregated and possibly supports the interior protection. The loading of Pt and Ni on the carbon support is 15 and 3 wt %, respectively, determined by ICP-OES.

In order to engineer their surface/near-surface structure, octahedral $Pt_{1.5}Ni$ nanoparticles and $Ni(NO_3)_2{\cdot}6H_2O$ were mixed and heated at 150 °C under 20% H_2/Ar (see schematic illustration in Scheme 1). During the heating, the Ni atoms reduced from $Ni(NO_3)_2{\cdot}6H_2O$ diffuse into the octahedral $Pt_{1.5}Ni$ nanocrystals.[54] Thus-obtained $Pt_{1.5}Ni$ with a modified surface/near-surface structure (MS-$Pt_{1.5}Ni$) shows the same XRD pattern as that of pristine $Pt_{1.5}Ni$ (Figure S4), which are both positively shifted compared with the standard pattern of Pt due to the additional introduction of Ni. MS-$Pt_{1.5}Ni$ exhibits

Scheme 1. Schematic Illustration of the Synthetic Route to A-$Pt_{1.5}Ni$, MS-$Pt_{1.5}Ni$, and A-MS-$Pt_{1.5}Ni$[a]

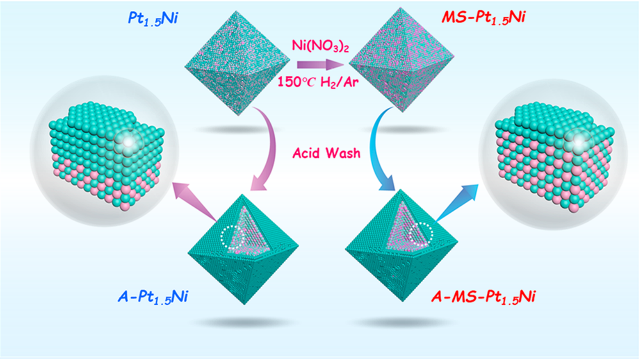

[a] The green spheres label Pt atoms, and the pink spheres label Ni atoms.

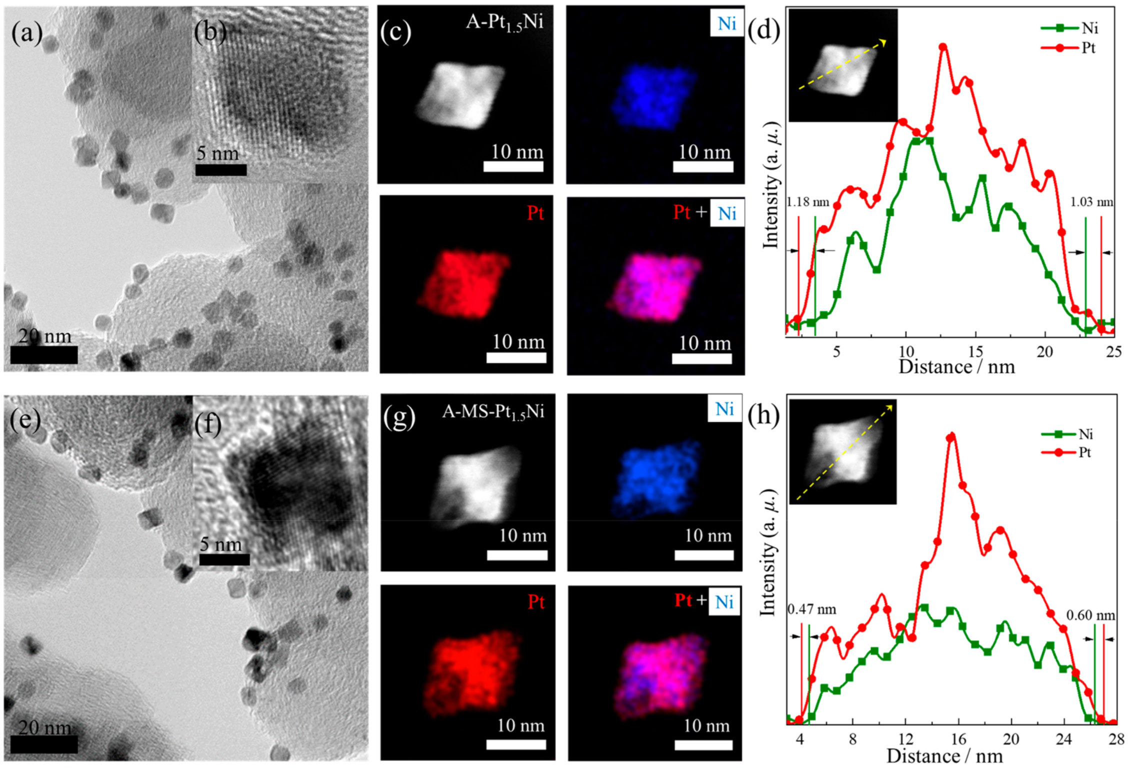

Figure 1. (a) TEM and (b) HR-TEM images of A-$Pt_{1.5}Ni$. (c) HAADF-STEM image and 2D EDS maps of Pt, Ni and overlapping in A-$Pt_{1.5}Ni$. (d) Line-scan EDS analysis of A-$Pt_{1.5}Ni$. (e) TEM and (f) HR-TEM images of A-MS-$Pt_{1.5}Ni$. (g) HAADF-STEM image and 2D EDS maps of Pt, Ni and overlapping in A-MS-$Pt_{1.5}Ni$. (h) Line-scan EDS analysis of A-MS-$Pt_{1.5}Ni$.

a modified electronic structure of Pt compared with $Pt_{1.5}Ni$ based on the XPS spectra, where Pt $4f_{7/2}$ peaks of MS-$Pt_{1.5}Ni$ shift negatively by 0.25 eV (Figure S3). This negative shift is due to the diffused Ni atoms with a lower electronegativity (1.92) compared with Pt (2.28). Even after the heating treatment, the MS-$Pt_{1.5}Ni$ nanoparticles are still well-dispersed on the carbon support and maintain their well-defined octahedral morphology (Figure S5). HAADF-STEM-EDS mapping (Figure S6) and line scan analysis (Figure S7) across a MS-$Pt_{1.5}Ni$ nanoparticle reveal that Pt and Ni are well-distributed throughout the octahedral nanocrystal. The bulk composition of MS-$Pt_{1.5}Ni$ is determined as $Pt_{56}Ni_{44}$ by EDS (shown in Figure S8 and Table S1).

Ni atoms on the surface were further leached by acid-immersing $Pt_{1.5}Ni$ and MS-$Pt_{1.5}Ni$ into 0.1 M $HClO_4$ for 12 h, which are denoted as A-$Pt_{1.5}Ni$ and A-MS-$Pt_{1.5}Ni$ (as shown in Scheme 1), respectively. Both A-$Pt_{1.5}Ni$ and A-MS-$Pt_{1.5}Ni$ are uniformly distributed on carbon support (shown in Figure 1a,e), and their octahedral shapes are also well maintained through the HR-TEM images (Figure 1b,f) even after the acid washing treatment. Based on HAADF-STEM-EDS of A-$Pt_{1.5}Ni$ (Figure 1c and Figure S9) and A-MS-$Pt_{1.5}Ni$ (Figure 1g and Figure S10), the surface/near-surface layers of A-$Pt_{1.5}Ni$ and A-MS-$Pt_{1.5}Ni$ are Pt-rich due to the stripping of surface Ni atoms during the acid washing process, while the interior maintains the Pt−Ni alloy. The elemental compositions of A-$Pt_{1.5}Ni$ and A-MS-$Pt_{1.5}Ni$ are determined as $Pt_{67}Ni_{33}$ and $Pt_{64}Ni_{36}$ by ICP-OES, as shown in Table S1. Furthermore, the Pt and Ni loadings of catalysts were also determined by ICP and shown in Table S2. The Pt layer thickness at near-surface of A-MS-$Pt_{1.5}Ni$ can be approximately two to three layers based on the calculation model, as shown in Figure S11 and Tables S3,S4. A detailed EDS-line scan was applied to finely detect the surface/near-surface at an atomic scale.[39,42] From the line scan profiles on A-$Pt_{1.5}Ni$ (Figure 1d and Figure S9e), the thickness of Pt-rich layers in A-$Pt_{1.5}Ni$, is determined to be five to eight atomic layers. In comparison, the thickness of the Pt-rich layer in A-MS-$Pt_{1.5}Ni$ (Figure 1h and Figure S10e) is reduced to two to three atomic layers.

Atomic-resolution HAADF-STEM was employed to determine the atomic surface structure. Figure 2a is the HAADF-STEM image of A-MS-$Pt_{1.5}Ni$. The atomic resolution STEM image of A-MS-$Pt_{1.5}Ni$ taken from the selected area marked by the yellow box in Figure 2a is shown in Figure 2b. Based on the different contrasts between Pt and Ni, the Ni atoms at near-surface are almost entirely replaced by Pt atoms, resulting in two to three Pt-rich layers (the atomical thin Pt-rich layers are highlighted by red dots), while a thick Pt-rich layer is found on the A-$Pt_{1.5}Ni$ (Figure 2c,d). The result from atomic resolution HAADF-STEM is consistent with that of line-scan EDS analysis. Compared with the traditional method of changing bulk composition, our surface engineering is an efficient method to atomically tune the surface structure of nanocatalysts without compromise of interior composition.

XPS spectra of A-$Pt_{1.5}Ni$ and A-MS-$Pt_{1.5}Ni$ with two different photon energies (1486.6 and 160.0 eV) are used to detect the surface/subsurface chemistry in different depths. When the photon energy is only 160.0 eV, the electronic structure of Pt atoms at the surface is detected as the detection depth is approximately 2−3 atomic layers (Figure 3a,b).[55] The Pt $4f_{7/2}$ peak of A-MS-$Pt_{1.5}Ni$ is located at 71.13 eV, whereas that of A-$Pt_{1.5}Ni$ is 71.23 eV. The negative shift of Pt 4f peak on A-MS-$Pt_{1.5}Ni$ indicates that the electronic structure of Pt atoms at the surface of A-MS-$Pt_{1.5}Ni$ is indeed modified by the

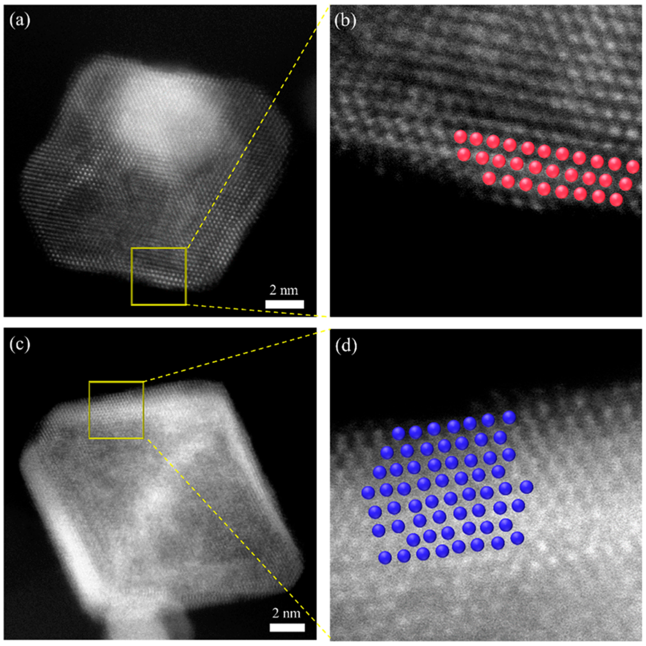

Figure 2. (a) HAADF-STEM image of a representative A-MS-$Pt_{1.5}Ni$ NP. (b) Atomic resolved HAADF image taken from the selected area indicated by the yellow box in (a). (c) HAADF-STEM image of a representative A-$Pt_{1.5}Ni$ NP. (d) Atomic-resolution HAADF image taken from the selected area indicated by the yellow box in (c).

near-surface diffused Ni atoms compared with A-$Pt_{1.5}Ni$. The conventional XPS spectra of A-MS-$Pt_{1.5}Ni$ and A-$Pt_{1.5}Ni$ (Figure S12), when the photon energy is 1486.6 eV, corresponding to the detection depth of about 10 atomic layers, show almost the identical Pt 4f peaks. This indicates that only Pt atoms at the surface are modified by the diffused Ni atoms, and the electronic effects are short-range in nature. This atomically precise control in terms of subsurface is based on the efficient modification approach proposed in our report.

The local electronic structure and atomic coordination of the catalysts are probed by X-ray absorption spectroscopy (XAS).[56] The Pt L_3- and L_2-edge XANES spectra of $Pt_{1.5}Ni$, MS-$Pt_{1.5}Ni$, and A-MS-$Pt_{1.5}Ni$ are shown in Figure 3c and Figure S13, respectively. The threshold energy (E_0) and first-derivative spectra (Figure S14) of Pt L_3-edge on $Pt_{1.5}Ni$, MS-$Pt_{1.5}Ni$, and A-MS-$Pt_{1.5}Ni$ are similar to those of Pt foil, confirming their metallic nature. Meanwhile, the Ni K edges in XANES spectra (Figure 3d) of Ni foil, $Pt_{1.5}Ni$, MS-$Pt_{1.5}Ni$, and A-MS-$Pt_{1.5}Ni$ also show similar features. The first-derivate spectra illustrate their metallic nature with an edge position of 8333 eV (Figure S15). The white line (WL) intensity of Pt L_3 (Figure 3c) and Pt L_2 (Figure S13) edges, as a qualitative indicator of electron vacancies in the 5d orbitals, shows the sequence: Pt foil ≤ MS-$Pt_{1.5}Ni$ < A-MS-$Pt_{1.5}Ni$ < $Pt_{1.5}Ni$. The changes in WL intensity could be caused by ligand effects, consistent with the XPS results. To fully understand the effect of the unoccupied densities of 5d states of these catalysts, quantitative WL intensity analysis was further conducted according to a reported method to determine the occupancy of the 5d states in each sample (see details in Experimental Section). The Pt L_3- and Pt L_2-edge threshold and WL parameters are summarized in Table 1. The unoccupied densities of 5d states of A-MS-$Pt_{1.5}Ni$ is different from that of

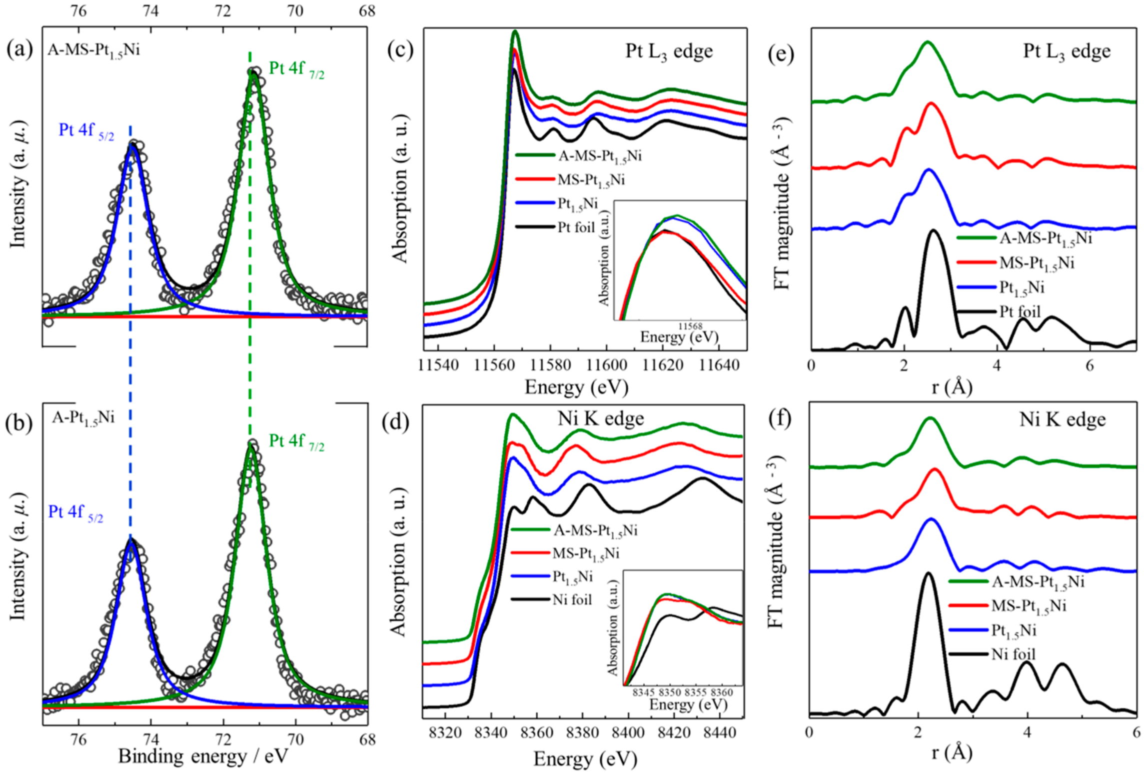

Figure 3. Synchrotron-based XPS spectra (photon energy is 160.0 eV) on A-MS-$Pt_{1.5}Ni$ (a) and A-$Pt_{1.5}Ni$ (b). Normalized XANES spectra of $Pt_{1.5}Ni$, MS-$Pt_{1.5}Ni$ and A-MS-$Pt_{1.5}Ni$ at Pt L_3 edge (c) and Ni K edge (d). EXAFS spectra of Pt $Pt_{1.5}Ni$, MS-$Pt_{1.5}Ni$ and A-MS-$Pt_{1.5}Ni$ at Pt L_3 edge (e) and Ni K edge (f).

Table 1. Pt L_3-Edge and Pt L_2-Edge WL Parameters

	Pt L_3-edge WL				Pt L_2-edge WL					
	E_0 (eV)[a]	E_{peak} (eV)[b]	Γ (eV)[c]	$\triangle A_3$[d]	E_0 (eV)[a]	E_{peak} (eV)[b]	Γ (eV)[c]	$\triangle A_2$	$h_{5/2}$	$h_{3/2}$
Pt foil	11564	11567.1	4	4.65187	13273	13276.2	2.39	2.58421	0.42587	0.12016
$Pt_{1.5}Ni$	11564	11567.3	4.47	5.13158	13273.2	13276.4	2.91	3.56203	0.46428	0.16563
MS- $Pt_{1.5}Ni$	11564.2	11567.2	4.31	5.06414	13273	13276.3	2.24	3.55006	0.45789	0.16507
A-MS-$Pt_{1.5}Ni$	11564.5	11567.5	4.59	5.08314	13273	13276	2.64	3.73321	0.45831	0.17831

[a] Position of the point of inflection of the rising edge. [b] Peak position. [c] Line width at half maximum of the WL. [d] Area under the difference curve for unity edge jump, the unity edge jump for the Pt L_3- and Pt L_2-edge corresponds to a value of 2.53×10^3 cm^{-1} and 1.163×10^3 cm^{-1}, respectively.

$Pt_{1.5}Ni$ and MS-$Pt_{1.5}Ni$ due to the ligand effect, which affects their activity in electrocatalytic reactions like ORR.[57]

The EXAFS spectra of Pt L_3- and Ni K-edges of $Pt_{1.5}Ni$, MS-$Pt_{1.5}Ni$ and A-MS-$Pt_{1.5}Ni$ are shown in Figure 3e,f. The corresponding fitting spectra are shown in Figures S16−S18, and the fitting parameters are given in Table S5. The Pt−Pt bond length of $Pt_{1.5}Ni$, MS-$Pt_{1.5}Ni$, and A-MS-$Pt_{1.5}Ni$ are shorter than that of Pt foil due to the incorporation of Ni atoms with smaller radius.[24] The same alloy effects lead to that the Ni−Ni bond length of $Pt_{1.5}Ni$, MS-$Pt_{1.5}Ni$, and A-MS-$Pt_{1.5}Ni$ is larger than that of pristine Ni foil (2.48 Å).

The electrocatalytic ORR performances of A-$Pt_{1.5}Ni$ and A-MS-$Pt_{1.5}Ni$ were evaluated using a rotating disk electrode (RDE). The commercial Pt/C and A-$Pt_{1.0}Ni$ (physical characterization shown in Figure S19) were also tested as reference samples. The CV curves of commercial Pt/C, A-$Pt_{1.5}Ni$, A-$Pt_{1.0}Ni$, and A-MS-$Pt_{1.5}Ni$ nanocatalysts were recorded in an argon saturated 0.1 M perchloric acid solution (Figure 4a). The onset potential of oxide formation for the A-MS-$Pt_{1.5}Ni$ nanocatalysts shifted positively versus that for Pt/C. Such a shift is representative of a less oxophilic catalyst surface on A-MS-$Pt_{1.5}Ni$ because of the modified electronic structure of surface Pt atoms by inner Ni.[58] The ECSA for all catalysts is shown in Table S6. For the purpose of probing the kinetic activity, a representative set of polarization curves for the ORR in oxygen saturated 0.1 M perchloric acid at the rotation rate of 1600 rpm are shown in Figure 4b. These polarization curves reveal that the ORR kinetics are accelerated on the octahedral A-MS-$Pt_{1.5}Ni$ surface. Compared with the commercial Pt/C, significant positive shifts of the half-wave potential by 60, 50, and 40 mV are observed on A-MS-$Pt_{1.5}Ni$, A-$Pt_{1.0}Ni$, and A-$Pt_{1.5}Ni$, respectively. Tafel plots (Figure S20) are consistent with the superior performance of A-MS-$Pt_{1.5}Ni$ and indicate the same ORR mechanism on these four catalysts based on the similar Tafel slopes.[59] As shown in Figure 4c, the specific activity of A-MS-$Pt_{1.5}Ni$ at 0.9 V is approximately 7.7 mA cm^{-2}, a 22-fold increase compared with Pt/C and ∼3-fold increase over both A-$Pt_{1.5}Ni$ and A-$Pt_{1.0}Ni$. In addition, the mass activity of A-MS-$Pt_{1.5}Ni$ (Figure 3d) shows a 4.3 times increase over the 2020 U.S. Department of Energy target (0.44 A $mg^{-1}{}_{Pt}$).

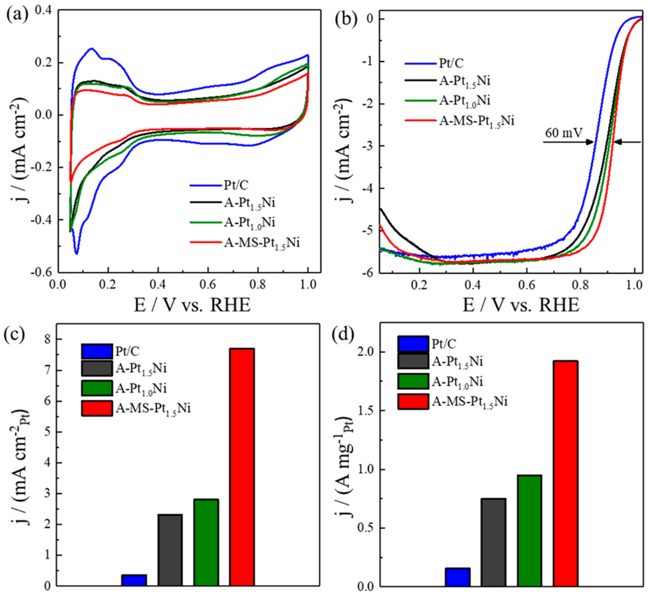

Figure 4. (a) CV of Pt/C, A-$Pt_{1.5}Ni$, A-$Pt_{1.0}Ni$, and A-MS-$Pt_{1.5}Ni$ in Ar-saturated 0.1 M $HClO_4$. (b) Polarization curves of Pt/C, A-$Pt_{1.5}Ni$, A-$Pt_{1.0}Ni$, and A-MS-$Pt_{1.5}Ni$ in O_2-saturated 0.1 M $HClO_4$ at a rotation rate of 1600 r min^{-1} (scan rate = 10 mV s^{-1}). Specific activities (c) and mass activities (d) at 0.9 V of Pt/C, A-$Pt_{1.5}Ni$, A-$Pt_{1.0}Ni$, and A-MS-$Pt_{1.5}Ni$.

DFT calculations were performed to rationalize the high ORR activity on A-MS-$Pt_{1.5}Ni$, which is not a traditional "Pt-skin" type electrocatalyst consisting of a full and smooth Pt monolayer or multilayers on extended Pt-M surfaces or nanoparticles through CO stripping curves shown in Figure S21,[9,25,37] probably because of its thermal treatment just at 150 °C and the leaching of Ni atoms. In regards to the predominant (111) planes on the surface of octahedra, periodic Pt (111), $Pt_{5\ ML}/Pt_{1.5}Ni$ (111)—five monolayers—and $Pt_{2\ ML}/Pt_{1.5}Ni$ (111)—two monolayers—were constructed as models of Pt/C, A-$Pt_{1.5}Ni$, and A-MS-$Pt_{1.5}Ni$, respectively. Density of electronic states on three models were calculated and are shown in Figure 5. The Pt−Pt bond length

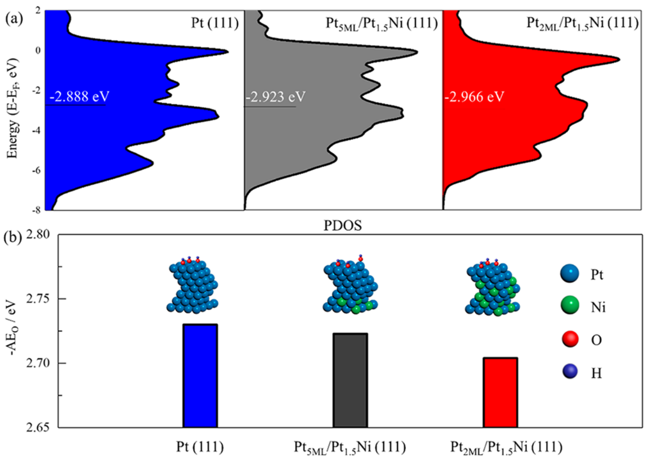

Figure 5. (a) Projected *d*-density of states of surface atoms on Pt (111), $Pt_{5\ ML}/Pt_{1.5}Ni$ (111), and $Pt_{2\ ML}/Pt_{1.5}Ni$ (111) slabs. (b) Binding energy of OH* on Pt (111), $Pt_{5\ ML}/Pt_{1.5}Ni$ (111), and $Pt_{2\ ML}/Pt_{1.5}Ni$ (111) slabs.

https://dx.doi.org/10.1021/acscatal.9b05133
ACS Catal. 2020, 10, 4205−4214

on surface of optimized Pt (111), $Pt_{5\ ML}/Pt_{1.5}Ni$ (111), and $Pt_{2\ ML}/Pt_{1.5}Ni$ (111) slabs is 2.775, 2.774, and 2.768 Å, respectively, demonstrating a significant compressive strain on $Pt_{2\ ML}/Pt_{1.5}Ni$ (111) compared with Pt (111) and $Pt_{5\ ML}/Pt_{1.5}Ni$ (111). The modified electronic structure, confirmed by XPS and WL analysis derived from XAFS, and geometric structure on A-MS-$Pt_{1.5}Ni$, might codetermine the remarkably enhanced ORR activity.

The *d* band center of $Pt_{2\ ML}/Pt_{1.5}Ni$ (111) surface is calculated to be −2.966 eV (shown in Figure 5a), showing a negative shift in comparison to Pt (111) (−2.888 eV) and $Pt_{5\ ML}/Pt_{1.5}Ni$ (111) (−2.923 eV) due to the ligand and strain effects. Based on the previously established *d*-band theory,[21,30,60] the downshifted *d*-band center could lower the adsorption energy of OH* on Pt, whose hydrogenation on Pt is the rate-determining step during ORR, resulting in greatly improved ORR activity. The adsorption energy of OH* ($\triangle E_0$) on Pt (111), $Pt_{5\ ML}/Pt_{1.5}Ni$ (111) and $Pt_{2\ ML}/Pt_{1.5}Ni$ (111) are calculated by DFT. $\triangle E_0$ on $Pt_{2\ ML}/Pt_{1.5}Ni$ (111) is only −2.704 eV, which is much lower than that on Pt (111) (−2.730 eV) and $Pt_{5\ ML}/Pt_{1.5}Ni$ (111) (−2.723 eV), leading to the enhanced ORR performance.

To evaluate the ORR durability of the catalysts, the ADTs were carried out between 0.6 and 1.0 V for 5000 cycles at a sweep rate of 50 mV s^{-1}. The CV curves and ORR polarization curves of different catalysts before and after ADTs were measured and shown in Figures S22, S23, and the derived ECSA values for all catalysts before and after stability test are shown in Table S7. For A-MS-$Pt_{1.5}Ni$ and A-$Pt_{1.5}Ni$, such ADTs cause only 9.2% and 8.5% loss of mass activity (Figure 6a,b), confirming that our near-surface engineering strategy effectively restrains their degradation. However, after the same tests, Pt/C and A-Pt_1Ni_1 loses strikingly 33% and 38% of their initial activity (Figure S23). Compositional and morphology changes that are due to the diffusion of interior Ni atoms and dissolution over the course of electrochemical stability testing have been usually considered as the main reason for poor stability.[27,41] The compositions before and after the stability tests, determined by ICP-OES, are shown in Table S8. The composition of A-Pt_1Ni_1 changes to $Pt_{75}Ni_{25}$ after ADTs. In contrast, there are only slight compositional changes for A-$Pt_{1.5}Ni$ and A-MS-$Pt_{1.5}Ni$, indicating the superior stability of the engineered samples. As revealed by HAADF-STEM-EDS shown in Figure 6a and Figures S24, S25, A-MS-$Pt_{1.5}Ni$ catalysts still maintains their well-defined octahedral shape after the ADTS, while A-Pt_1Ni nanoparticles lose their octahedral shape (Figure S26) because of the dissolution of Ni atoms. A longer stability test including 10 000 cycles as shown in Figure S27 also indicates the robust stability of A-MS-$Pt_{1.5}Ni$. Our near-surface atomically engineered octahedral $Pt_{1.5}Ni$ alloy excels most Pt−Ni nanocatalysts in terms of activity and stability (shown in Figures S28−30).

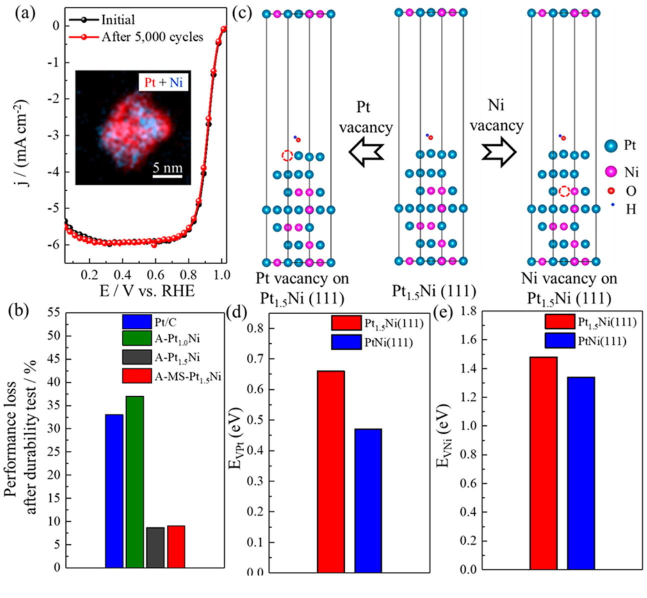

Figure 6. (a) Polarization curves of A-MS-$Pt_{1.5}Ni$ in oxygen saturated 0.1 $HClO_4$ before and after 5000 potential cycles between 0.6 and 1.0 V versus RHE (the inset image is the EDS element maps of Pt and Ni after stability test). (b) Mass activity loss after durability test on Pt/C, A-$Pt_{1.5}Ni$, A-$Pt_{1.0}Ni$ and A-MS-$Pt_{1.5}Ni$. (c) The theoretical models of formation of Pt atom vacancy at surface and interior Ni atom vacancy of $Pt_{1.5}Ni$ (111) (d) Pt and (e) Ni vacancy formation energies for $Pt_{1.5}Ni$ (111) and $Pt_{1.0}Ni$ (111).

It is interesting that A-MS-$Pt_{1.5}Ni$ with an ultrathin Pt-rich layer (~two atomic layers) shows a robust stability because Pt−Ni octahedra with a thin Pt-rich surface layer usually present a poor stability, such as A-$Pt_{1.0}Ni$. The enhanced stability on A-MS-$Pt_{1.5}Ni$ may be attributed to the difference of interior composition, where our surface engineering method enables an ultrathin Pt-rich layer on Pt-rich PtNi composition, which cannot be achieved by conventional (electro)chemical leaching. DFT calculations were performed to shed light on the high stability and correlate the interior composition with stability. The vacancy formation energy of surface Pt atoms (E_{VPt}) and interior Ni atoms (E_{VNi}) can be considered as a descriptor to reflect the durability of Pt−Ni octahedra catalysts because the dissolution of surface Pt atoms and diffusion of interior Ni atoms results in the deactivation of catalysts.[61] The E_{VPt} and E_{VNi} on $Pt_{1.5}Ni$ (111) and PtNi (111) with two layers of surface Pt atoms are compared, where the theoretic models are shown in Figure 6c and Figures S31, S32. The E_{VPt} and E_{VNi} on $Pt_{1.5}Ni$ (111) are obviously higher than those on PtNi (111) (shown in Figure 6d,e), demonstrating Pt-rich composition could stabilize both surface Pt atoms and subsurface Ni atoms. Thus, the interior Pt-rich composition leads to a robust durability on A-MS-$Pt_{1.5}Ni$ with ultrathin Pt-rich surface layers.

■ CONCLUSION

The atomical engineering of surface/near-surface for shape-selective $Pt_{1.5}Ni$ nanoparticles is demonstrated as an effective strategy for their performance improvement. After the surface modification, the Pt-rich layers are reduced to two atomic layers, leading to further modified electronic and geometric structures as verified through synchrotron-based XPS, WL analysis derived from XANES, and DFT. DFT calculations reveal a negative shift of the d-band center and a weaker adsorption of OH* on A-MS-$Pt_{1.5}Ni$. Therefore, the A-MS-$Pt_{1.5}Ni$ nanocatalyst achieves a factor of 20 enhancement in specific activity and a factor of 10 enhancement in mass activity, compared with commercial Pt/C. Meanwhile, the modified catalyst shows a robust stability even with the ultrathin surface Pt layers, as the compositional nature of A-MS-$Pt_{1.5}Ni$ could prevent Ni diffusion and dissolution as confirmed by DFT calculations and ICP-OES. We believe that this near-surface engineering strategy is a promising step in the design of shaped Pt−Ni catalysts and next-generation catalysts for ORR and other electrochemical reactions.

ASSOCIATED CONTENT

Supporting Information

The Supporting Information is available free of charge at https://pubs.acs.org/doi/10.1021/acscatal.9b05133.

> TEM and HR-TEM images, XPS spectra, XRD patterns, HAADF-STEM-EDS images and line-scan analysis, XANES spectra and EXAFS fitting results, stability test and Tafel plots, CO stripping curves, ORR polarization curves, composition (PDF)

AUTHOR INFORMATION

Corresponding Authors

Chunyu Du − *MIIT Key Laboratory of Critical Materials Technology for New Energy Conversion and Storage, Harbin Institute of Technology, Harbin 150001, China;* orcid.org/0000-0003-0547-7724; Email: cydu@hit.edu.cn

Jun Luo − *Ceter for Electron Microscopy and Tianjin Key Lab of Advanced Functional Porous Materials, Institute for New Energy Materials and Low-Carbon Technologies, School of Materials Science and Engineering, Tianjin University of Technology, Tianjin 300384, China;* orcid.org/0000-0001-5084-2087; Email: jluo@tjut.edu.cn

Xueliang Sun − *Department of Mechanical and Materials Engineering, University of Western Ontario, London, Ontario N6A 5B9, Canada;* orcid.org/0000-0003-0374-1245; Email: xsun9@uwo.ca

Authors

Fanpeng Kong − *MIIT Key Laboratory of Critical Materials Technology for New Energy Conversion and Storage, Harbin Institute of Technology, Harbin 150001, China; Department of Mechanical and Materials Engineering, University of Western Ontario, London, Ontario N6A 5B9, Canada*

Zhouhong Ren − *Ceter for Electron Microscopy and Tianjin Key Lab of Advanced Functional Porous Materials, Institute for New Energy Materials and Low-Carbon Technologies, School of Materials Science and Engineering, Tianjin University of Technology, Tianjin 300384, China*

Mohammad Norouzi Banis − *Department of Mechanical and Materials Engineering, University of Western Ontario, London, Ontario N6A 5B9, Canada;* orcid.org/0000-0002-6144-6837

Lei Du − *MIIT Key Laboratory of Critical Materials Technology for New Energy Conversion and Storage, Harbin Institute of Technology, Harbin 150001, China;* orcid.org/0000-0001-9584-4748

Xin Zhou − *MIIT Key Laboratory of Critical Materials Technology for New Energy Conversion and Storage, Harbin Institute of Technology, Harbin 150001, China*

Guangyu Chen − *MIIT Key Laboratory of Critical Materials Technology for New Energy Conversion and Storage, Harbin Institute of Technology, Harbin 150001, China*

Lei Zhang − *Department of Mechanical and Materials Engineering, University of Western Ontario, London, Ontario N6A 5B9, Canada*

Junjie Li − *Department of Mechanical and Materials Engineering, University of Western Ontario, London, Ontario N6A 5B9, Canada*

Sizhe Wang − *Department of Mechanical and Materials Engineering, University of Western Ontario, London, Ontario N6A 5B9, Canada*

Minsi Li − *Department of Mechanical and Materials Engineering, University of Western Ontario, London, Ontario N6A 5B9, Canada*

Kieran Doyle-Davis − *Department of Mechanical and Materials Engineering, University of Western Ontario, London, Ontario N6A 5B9, Canada*

Yulin Ma − *MIIT Key Laboratory of Critical Materials Technology for New Energy Conversion and Storage, Harbin Institute of Technology, Harbin 150001, China*

Ruying Li − *Department of Mechanical and Materials Engineering, University of Western Ontario, London, Ontario N6A 5B9, Canada*

Alan Young − *Ballard Power Systems Inc., Burnaby, British Columbia V5J 5J8, Canada*

Lijun Yang − *Ballard Power Systems Inc., Burnaby, British Columbia V5J 5J8, Canada*

Matthew Markiewicz − *Ballard Power Systems Inc., Burnaby, British Columbia V5J 5J8, Canada*

Yujin Tong − *Fritz Haber Institute of the Max Planck Society, Berlin 14195, Germany;* orcid.org/0000-0002-4084-7711

Geping Yin − *MIIT Key Laboratory of Critical Materials Technology for New Energy Conversion and Storage, Harbin Institute of Technology, Harbin 150001, China;* orcid.org/0000-0002-8804-6550

Complete contact information is available at: https://pubs.acs.org/10.1021/acscatal.9b05133

Author Contributions

[#]F.P.K., Z.H.R., and M.N.B. contributed equally.

Notes

The authors declare no competing financial interest.

ACKNOWLEDGMENTS

This work is supported by National Natural Science Foundation of China (Grant Nos. 21433003, 21773049, and 51761165012), Natural Sciences and Engineering Research Council of Canada (NSERC), Canada Research Chair (CRC) Program, Canada Foundation for Innovation (CFI), Ballard Power Systems Inc., Canadian Light Source (CLS), the University of Western Ontario, and the 111 project of China (D17003). F.P.K. also acknowledges financial support from the China Scholarship Council.

REFERENCES

(1) Gasteiger, H. A.; Markovic, N. M. Just a Dream-or Future Reality? *Science* **2009**, *324*, 48−49.

(2) Stephens, I. E. L.; Rossmeisl, J.; Chorkendorff, I. Toward Sustainable Fuel Cells. *Science* **2016**, *354*, 1378−1379.

(3) Tian, N.; Lu, B.; Yang, X.; Huang, R.; Jiang, Y.; Zhou, Z.; Sun, S. Rational Design and Synthesis of Low-Temperature Fuel Cell Electrocatalysts. *Electrochem. Energy Rev.* **2018**, *1*, 54−83.

(4) Shao, M.; Chang, Q.; Dodelet, J. P.; Chenitz, R. Recent Advances in Electrocatalysts for Oxygen Reduction Reaction. *Chem. Rev.* **2016**, *116*, 3594−657.

(5) Shao, M. H.; Shoemaker, K.; Peles, A.; Kaneko, K.; Protsailo, L. Pt Mono layer on Porous Pd-Cu Alloys as Oxygen Reduction Electrocatalysts. *J. Am. Chem. Soc.* **2010**, *132*, 9253−9255.

(6) Escudero-Escribano, M.; Malacrida, P.; Hansen, M. H.; Vej-Hansen, U. G.; Velazquez-Palenzuela, A.; Tripkovic, V.; Schiotz, J.; Rossmeisl, J.; Stephens, I. E.; Chorkendorff, I. Tuning the Activity of

Pt Alloy Electrocatalysts by Means of the Lanthanide Contraction. *Science* **2016**, *352*, 73−76.

(7) Zhao, X.; Chen, S.; Fang, Z. C.; Ding, J.; Sang, W.; Wang, Y. C.; Zhao, J.; Peng, Z. M.; Zeng, J. Octahedral Pd@$Pt_{1.8}$Ni Core-Shell Nanocrystals with Ultrathin PtNi Alloy Shells as Active Catalysts for Oxygen Reduction Reaction. *J. Am. Chem. Soc.* **2015**, *137*, 2804−2807.

(8) Wang, R.; Wang, H.; Luo, F.; Liao, S. Core−Shell-Structured Low-Platinum Electrocatalysts for Fuel Cell Applications. *Electrochem. Energy Rev.* **2018**, *1*, 324−387.

(9) Stamenkovic, V. R.; Mun, B. S.; Arenz, M.; Mayrhofer, K. J. J.; Lucas, C. A.; Wang, G.; Ross, P. N.; Markovic, N. M. Trends in Electrocatalysis on Extended and Nanoscale Pt-Bimetallic Alloy Surfaces. *Nat. Mater.* **2007**, *6*, 241−247.

(10) Koh, S.; Strasser, P. Electrocatalysis on Bimetallic Surfaces: Modifying Catalytic Reactivity for Oxygen Reduction by Voltammetric Surface Dealloying. *J. Am. Chem. Soc.* **2007**, *129*, 12624−12625.

(11) Wang, D. L.; Xin, H. L. L.; Hovden, R.; Wang, H. S.; Yu, Y. C.; Muller, D. A.; DiSalvo, F. J.; Abruna, H. D. Structurally Ordered Intermetallic Platinum-Cobalt Core-Shell Nanoparticles with Enhanced Activity and Stability as Oxygen Reduction Electrocatalysts. *Nat. Mater.* **2013**, *12*, 81−87.

(12) Guo, S.; Li, D.; Zhu, H.; Zhang, S.; Markovic, N. M.; Stamenkovic, V. R.; Sun, S. FePt and CoPt Nanowires as Efficient Catalysts for the Oxygen Reduction Reaction. *Angew. Chem., Int. Ed.* **2013**, *52*, 3465−3468.

(13) Jaouen, F.; Jones, D.; Coutard, N.; Artero, V.; Strasser, P.; Kucernak, A. Toward Platinum Group Metal-Free Catalysts for Hydrogen/Air Proton-Exchange Membrane Fuel Cells. *Johnson Matthey Technol. Rev.* **2018**, *62*, 231−255.

(14) Osmieri, L. TransitionMetal−Nitrogen−Carbon (M−N−C) Catalysts for Oxygen Reduction Reaction. Insights on Synthesis and Performance in Polymer Electrolyte Fuel Cells. *Chemengineering* **2019**, *3*, 16.

(15) Banham, D.; Choi, J. Y.; Kishimoto, T.; Ye, S. Y. Integrating PGM-Free Catalysts into Catalyst Layers and Proton Exchange Membrane Fuel Cell Devices. *Adv. Mater.* **2019**, *31*, 1804846.

(16) Calle-Vallejo, F.; Tymoczko, J.; Colic, V.; Vu, Q. H.; Pohl, M. D.; Morgenstern, K.; Loffreda, D.; Sautet, P.; Schuhmann, W.; Bandarenka, A. S. Finding Optimal Surface sites on Heterogeneous Catalysts by Counting Nearest Neighbors. *Science* **2015**, *350*, 185.

(17) Markovic, N.; Gasteiger, H.; Ross, P. Oxygen Reduction on Platinum Low-Index Single-Crystal Surfaces in Sulfuric Acid Solution − Rotating Ring Pt(hkl) Disk Studies. *J. Phys. Chem.* **1995**, *99*, 3411−3415.

(18) Martinez-Rodriguez, R.; Vidal-Iglesias, F.; Solla-Gullon, J.; Cabrera, C.; Feliu, J. Synthesis of Pt Nanoparticles in Water-in-Oil Microemulsion: Effect of HCl on Their Surface Structure. *J. Am. Chem. Soc.* **2014**, *136*, 1280−1283.

(19) Kang, Y.; Li, M.; Cai, Y.; Cargnello, M.; Diaz, R.; Gordon, T.; Wieder, N.; Adzic, R.; Gorte, R.; Stach, E.; Murray, C. Heterogeneous Catalysts Need Not Be so "Heterogeneous": Monodisperse Pt Nanocrystals by Combining Shape-Controlled Synthesis and Purification by Colloidal Recrystallization. *J. Am. Chem. Soc.* **2013**, *135*, 2741−2747.

(20) Wang, C.; Daimon, H.; Lee, Y.; Kim, J.; Sun, S. Synthesis of Monodisperse Pt Nanocubes and Their Enhanced Catalysis for Oxygen Reduction. *J. Am. Chem. Soc.* **2007**, *129*, 6974−6975.

(21) Stamenkovic, V.; Mun, B.; Mayrhofer, K.; Ross, P.; Markovic, N.; Rossmeisl, J.; Greeley, J.; Norskov, J. Changing the Activity of Electrocatalysts for Oxygen Reduction by Tuning the Surface Electronic Structure. *Angew. Chem., Int. Ed.* **2006**, *45*, 2897−2901.

(22) Zhang, J.; Vukmirovic, M.; Xu, Y.; Mavrikakis, M.; Adzic, R. Controlling the Catalytic Activity of Platinum-Monolayer Electrocatalysts for Oxygen Reduction with Different Substrates. *Angew. Chem., Int. Ed.* **2005**, *44*, 2132−2135.

(23) Wang, X.; Choi, S. I.; Roling, L. T.; Luo, M.; Ma, C.; Zhang, L.; Chi, M.; Liu, J.; Xie, Z.; Herron, J. A.; Mavrikakis, M.; Xia, Y. Palladium-Platinum Core-Shell Icosahedra with Substantially Enhanced Activity and Durability towards Oxygen Reduction. *Nat. Commun.* **2015**, *6*, 7594.

(24) Chen, G.; Kuttiyiel, K. A.; Su, D.; Li, M.; Wang, C.-H.; Buceta, D.; Du, C.; Gao, Y.; Yin, G.; Sasaki, K.; Vukmirovic, M. B.; Adzic, R. R. Oxygen Reduction Kinetics on Pt Monolayer Shell Highly Affected by the Structure of Bimetallic AuNi Cores. *Chem. Mater.* **2016**, *28*, 5274−5281.

(25) Chen, C.; Kang, Y.; Huo, Z.; Zhu, Z.; Huang, W.; Xin, H. L.; Snyder, J. D.; Li, D.; Herron, J. A.; Mavrikakis, M.; Chi, M.; More, K. L.; Li, Y.; Markovic, N. M.; Somorjai, G. A.; Yang, P.; Stamenkovic, V. R. Highly Crystalline Multimetallic Nanoframes with Three-Dimensional Electrocatalytic Surfaces. *Science* **2014**, *343*, 1339−1343.

(26) Becknell, N.; Son, Y.; Kim, D.; Li, D. G.; Yu, Y.; Niu, Z. Q.; Lei, T.; Sneed, B. T.; More, K. L.; Markovic, N. M.; Stamenkovic, V. R.; Yang, P. D. Control of Architecture in Rhombic Dodecahedral Pt−Ni Nanoframe Electrocatalysts. *J. Am. Chem. Soc.* **2017**, *139*, 11678−11681.

(27) Huang, X.; Zhao, Z.; Cao, L.; Chen, Y.; Zhu, E.; Lin, Z.; Li, M.; Yan, A.; Zettl, A.; Wang, Y.; Duan, X.; Mueller, T.; Huang, Y. High-Performance Transition Metal-Doped Pt_3Ni Octahedra for Oxygen Reduction Reaction. *Science* **2015**, *348*, 1230−1234.

(28) Schlapka, A.; Lischka, M.; Groβ, A.; Kasberger, U.; Jakob, P. Surface Strain versus Substrate Interaction in Heteroepitaxial Metal Layers: Pt on Ru(0001). *Phys. Rev. Lett.* **2003**, *91*, 016101.

(29) Ruban, A.; Hammer, B.; Stoltze, P.; Skriver, H.; Norskov, J. Surface Electronic Structure and Reactivity of Transition and Noble Metals. *J. Mol. Catal. A: Chem.* **1997**, *115*, 421−429.

(30) Kitchin, J.; Norskov, J.; Barteau, M.; Chen, J. Role of Strain and Ligand Effects in the Modification of the Electronic and Chemical Properties of Bimetallic Surfaces. *Phys. Rev. Lett.* **2004**, *93*, 156801.

(31) Jia, Q.; Segre, C.; Ramaker, D.; Caldwell, K.; Trahan, M.; Mukerjee, S. Structure-Property-Activity Correlations of Pt-Bimetallic Nanoparticles: A Theoretical Study. *Electrochim. Acta* **2013**, *88*, 604−613.

(32) Stamenkovic, V. R.; Fowler, B.; Mun, B. S.; Wang, G.; Ross, P. N.; Lucas, C. A.; Markovic, N. M. Improved Oxygen Reduction Activity on Pt_3Ni(111) via Increased Surface Site Availability. *Science* **2007**, *315*, 493−497.

(33) Cui, C.; Gan, L.; Li, H. H.; Yu, S. H.; Heggen, M.; Strasser, P. Octahedral PtNi Nanoparticle Catalysts: Exceptional Oxygen Reduction Activity by Tuning the Alloy Particle Surface Composition. *Nano Lett.* **2012**, *12*, 5885−5889.

(34) Zhang, J.; Yang, H. Z.; Fang, J. Y.; Zou, S. Z. Synthesis and Oxygen Reduction Activity of Shape-Controlled Pt_3Ni Nanopolyhedra. *Nano Lett.* **2010**, *10*, 638−644.

(35) Choi, S. I.; Xie, S.; Shao, M.; Odell, J. H.; Lu, N.; Peng, H. C.; Protsailo, L.; Guerrero, S.; Park, J.; Xia, X.; Wang, J.; Kim, M. J.; Xia, Y. Synthesis and Characterization of 9 nm Pt-Ni Octahedra with A Record High Activity of 3.3 A/mg_{Pt} for the Oxygen Reduction Reaction. *Nano Lett.* **2013**, *13*, 3420−3425.

(36) Zhang, C.; Hwang, S. Y.; Trout, A.; Peng, Z. Solid-State Chemistry-Enabled Scalable Production of Octahedral Pt-Ni Alloy Electrocatalyst for Oxygen Reduction Reaction. *J. Am. Chem. Soc.* **2014**, *136*, 7805−7808.

(37) Cui, C.; Gan, L.; Heggen, M.; Rudi, S.; Strasser, P. Compositional Segregation in Shaped Pt Alloy Nanoparticles and Their Structural Behaviour during Electrocatalysis. *Nat. Mater.* **2013**, *12*, 765−771.

(38) Park, J.; Liu, J. Y.; Peng, H. S.; Figueroa-Cosme, L.; Miao, S.; Choi, S.; Bao, X. S.; Yang, X.; Xia, Y. N. Coating Pt-Ni Octahedra with Ultrathin Pt Shells to Enhance the Durability without Compromising the Activity toward Oxygen Reduction. *ChemSusChem* **2016**, *9*, 2209−2215.

(39) Wang, C.; Chi, M.; Li, D.; Strmcnik, D.; van der Vliet, D.; Wang, G.; Komanicky, V.; Chang, K.-C.; Paulikas, A. P.; Tripkovic, D.; Pearson, J.; More, K. L.; Markovic, N. M.; Stamenkovic, V. R. Design and Synthesis of Bimetallic Electrocatalyst with Multilayered Pt-Skin Surfaces. *J. Am. Chem. Soc.* **2011**, *133*, 14396−14403.

(40) Dubau, L.; Asset, T.; Chattot, R.; Bonnaud, C.; Vanpeene, V.; Nelayah, J.; Maillard, F. Tuning the Performance and the Stability of Porous Hollow PtNi/C Nanostructures for the Oxygen Reduction Reaction. *ACS Catal.* **2015**, *5*, 5333−5341.

(41) Mayrhofer, K.; Hartl, K.; Juhart, V.; Arenz, M. Degradation of Carbon-Supported Pt Bimetallic Nanoparticles by Surface Segregation. *J. Am. Chem. Soc.* **2009**, *131*, 16348−16349.

(42) Li, J.; Xi, Z.; Pan, Y. T.; Spendelow, J. S.; Duchesne, P. N.; Su, D.; Li, Q.; Yu, C.; Yin, Z.; Shen, B.; Kim, Y. S.; Zhang, P.; Sun, S. Fe Stabilization by Intermetallic L_{10}-FePt and Pt Catalysis Enhancement in L_{10}-FePt/Pt Nanoparticles for Efficient Oxygen Reduction Reaction in Fuel Cells. *J. Am. Chem. Soc.* **2018**, *140*, 2926−2932.

(43) Li, J.; Sharma, S.; Liu, X.; Pan, Y.; Spendelow, J.; Chi, M.; Jia, Y.; Zhang, P.; Cullen, D.; Xi, Z.; Lin, H.; Yin, Z.; Shen, B.; Muzzio, M.; Yu, C.; Kim, Y.; Peterson, A.; More, K.; Zhu, H.; Sun, S. Hard-Magnet L10-CoPt Nanoparticles Advance Fuel Cell Catalysis. *Joule* **2019**, *3*, 124−135.

(44) Beermann, V.; Gocyla, M.; Kuehl, S.; Padgett, E.; Schmies, H.; Goerlin, M.; Erini, N.; Shviro, M.; Heggen, M.; Dunin-Borkowski, R.; Muller, D.; Strasser, P. Tuning the Electrocatalytic Oxygen Reduction Reaction Activity and Stability of Shape-Controlled Pt-Ni Nanoparticles by Thermal Annealing Elucidating the Surface Atomic Structural and Compositional Changes. *J. Am. Chem. Soc.* **2017**, *139*, 16536−16547.

(45) Ravel, B.; Newville, M. ATHENA, ARTEMIS, HEPHAESTUS: Data Analysis for X-ray Absorption Spectroscopy using IFEFFIT. *J. Synchrotron Radiat.* **2005**, *12*, 537−541.

(46) Cheng, N.; Norouzi Banis, M.; Liu, J.; Riese, A.; Mu, S.; Li, R.; Sham, T. K.; Sun, X. Atomic Scale Enhancement of Metal−Support Interactions between Pt and ZrC for Highly Stable Electrocatalysts. *Energy Environ. Sci.* **2015**, *8*, 1450−1455.

(47) Cheng, N.; Stambula, S.; Wang, D.; Banis, M. N.; Liu, J.; Riese, A.; Xiao, B.; Li, R.; Sham, T. K.; Liu, L. M.; Botton, G. A.; Sun, X. Platinum Single-Atom and Cluster Catalysis of the Hydrogen Evolution Reaction. *Nat. Commun.* **2016**, *7*, 13638.

(48) Sham, T. K.; Naftel, S. J.; Coulthard, I. M(3,2)-edge X-Ray Absorption Near-Edge Structure Spectroscopy: An Alternative Probe to the L(3,2)-Edge Near-Edge Structure for the Unoccupied Densities of d States of 5d Metals. *J. Appl. Phys.* **1996**, *79*, 7134−7138.

(49) Kresse, G.; Furthmüller, J. Efficient Iterative Schemes for Ab Initio Total-Energy Calculations Using A Plane-Wave Basis Set. *Phys. Rev. B: Condens. Matter Mater. Phys.* **1996**, *54*, 11169−11186.

(50) Kresse, G.; Hafner, J. Ab-initio Molecular-Dynamics Simulation of the Liquid-Metal Amorphous-Semiconductor Transition in Germanium. *Phys. Rev. B: Condens. Matter Mater. Phys.* **1994**, *49*, 14251−14269.

(51) Blöchl, P. E. Projected Augmented-Wave Method. *Phys. Rev. B: Condens. Matter Mater. Phys.* **1994**, *50*, 17953−17979.

(52) Perdew, J. P.; Burke, K.; Ernzerhof, M. Generalized Gradient Approximation Made Simple. *Phys. Rev. Lett.* **1996**, *77*, 3865−3868.

(53) Monkhorst, H. J.; Pack, J. D. Special Points for Brillouin-Zone Integrations. *Phys. Rev. B* **1976**, *13*, 5188.

(54) Oezaslan, M.; Hasche, F.; Strasser, P. In Situ Observation of Bimetallic Alloy Nanoparticle Formation and Growth Using High-Temperature XRD. *Chem. Mater.* **2011**, *23*, 2159−2165.

(55) Tanuma, S.; Powell, C.; Penn, D. Calculations of Electron Inelastic Mean Free Paths. 2. Data for 27 Elements over the 50 - 2 000 eV Range. Surf. Interface Anal. *Surf. Interface Anal.* **1991**, *17*, 911−926.

(56) Becknell, N.; Kang, Y.; Chen, C.; Resasco, J.; Kornienko, N.; Guo, J.; Markovic, N. M.; Somorjai, G. A.; Stamenkovic, V. R.; Yang, P. Atomic Structure of Pt_3Ni Nanoframe Electrocatalysts by in Situ X-ray Absorption Spectroscopy. *J. Am. Chem. Soc.* **2015**, *137*, 15817−15824.

(57) Chen, S.; Sheng, W. C.; Yabuuchi, N.; Ferreira, P. J.; Allard, L. F.; Shao-Horn, Y. Origin of Oxygen Reduction Reaction Activity on ″Pt_3Co″ Nanoparticles: Atomically Resolved Chemical Compositions and Structures. *J. Phys. Chem. C* **2009**, *113*, 1109−1125.

(58) Strasser, P.; Koh, S.; Anniyev, T.; Greeley, J.; More, K.; Yu, C. F.; Liu, Z. C.; Kaya, S.; Nordlund, D.; Ogasawara, H.; Toney, M. F.; Nilsson, A. Lattice-Strain Control of the Activity in Dealloyed Core-Shell Fuel Cell Catalysts. *Nat. Chem.* **2010**, *2*, 454−460.

(59) Stamenkovic, V.; Schmidt, T.; Ross, P.; Markovic, N. Surface Segregation Effects in Electrocatalysis: Kinetics of Oxygen Reduction Reaction on Polycrystalline Pt_3Ni Alloy Surfaces. *J. Electroanal. Chem.* **2003**, *554*, 191−199.

(60) Norskov, J.; Bligaard, T.; Rossmeisl, J.; Christensen, C. Towards the Computational Design of Solid Catalysts. *Nat. Chem.* **2009**, *1*, 37−46.

(61) Li, K.; Li, X. X.; Huang, H. W.; Luo, L. H.; Li, X.; Yan, X. P.; Ma, C.; Si, R.; Yang, J. L.; Zeng, J. One-Nanometer-Thick PtNiRh Trimetallic Nanowires with Enhanced Oxygen Reduction Electrocatalysis in Acid Media: Integrating Multiple Advantages into One Catalyst. *J. Am. Chem. Soc.* **2018**, *140*, 16159−16167.